



OPEN

Large-Scale, Three-Dimensional, Free-Standing, and Mesoporous Metal Oxide Networks for High-Performance Photocatalysis

SUBJECT AREAS:

NANOWIRES

NANOPARTICLES

SYNTHESIS AND PROCESSING

SOLID-STATE CHEMISTRY

Hua Bai, Xinshi Li, Chao Hu, Xuan Zhang, Junfang Li, Yan Yan & Guangcheng Xi

Received
22 April 2013Accepted
31 May 2013Published
16 July 2013

Correspondence and requests for materials should be addressed to G.C.X. (xiguangcheng@caiq.gov.cn)

Inspection and Research Center of Nanomaterials and Nanoproducts, Chinese Academy of Inspection and Quarantine, No. A3, North Route, Gaobeidian, Chaoyang District, Beijing, 100123, P. R. China.

Mesoporous nanostructures represent a unique class of photocatalysts with many applications, including splitting of water, degradation of organic contaminants, and reduction of carbon dioxide. In this work, we report a general Lewis acid catalytic template route for the high-yield producing single- and multi-component large-scale three-dimensional (3D) mesoporous metal oxide networks. The large-scale 3D mesoporous metal oxide networks possess large macroscopic scale (millimeter-sized) and mesoporous nanostructure with huge pore volume and large surface exposure area. This method also can be used for the synthesis of large-scale 3D macro/mesoporous hierarchical porous materials and noble metal nanoparticles loaded 3D mesoporous networks. Photocatalytic degradation of Azo dyes demonstrated that the large-scale 3D mesoporous metal oxide networks enable high photocatalytic activity. The present synthetic method can serve as the new design concept for functional 3D mesoporous nanomaterials.

Metal oxides have found applications in catalysis, sensors, solid oxide fuel cells, solar cells, and photocatalysis^{1–9}. The porous structures with high specific surface areas can greatly improve the performance of the metal oxides^{10–12}. For example, mesoporous TiO₂ materials with large surface area have shown high efficiency in dye-sensitized solar cells¹³. B/N doping mesoporous TiO₂ nanostructures possess enhanced visible-light photocatalytic performance¹⁴. Mesoporous Co₃O₄ nanowires display high capacity and rate capability in lithium ion batteries¹⁵. Various template-based synthetic strategies have been reported for the preparation of porous materials, including soft ones such as gas bubbles, surfactants, emulsion droplets, micelles, vesicles, and hard ones, such as mesoporous silica, polystyrene spheres, carbonate microcrystals, and carbonaceous spheres^{16–19}. Besides the template methods, solution-phase template-free methods including galvanic replacement, Kirkendall process, and sol-gel method, have also been developed by carefully tailoring the formation process of porous structures^{20–23}. Despite these successes, a general, economical, and scalable route to rationally fabricate large-scale 3D mesoporous materials with controllable shapes and sizes is still a challenge and highly desirable. Clearly, a method that can produce large-scale 3D mesoporous structures for a wide variety of materials is of particular significance.

Furfural alcohol (FA) has been used as a source for carbon materials, as it is readily available and easy to control²⁴. Besides strong acid, it has been known that some Lewis acid also can catalyze furfural alcohol resulting furfural alcohol resin (FAR)²⁵. Upon heating in air, FAR undergoes successive reactions, that is, polymerization, carbonization, and combustion. Inspired by these features, a facile FA-template method was design to synthesize large-scale 3D mesoporous metal oxide networks. Our inspiration raise from the following idea: for most metal elements, their cations can be thought of as Lewis acids. Therefore, we can use the metal salts as Lewis acids to catalyze FA resulting metal/FAR hybrids. The furfural alcohol acts as both the fuel and a transforming template, leading to the formation of 3D porous metal oxides by combustion reaction.

Herein, we describe a general, scalable, and reproducible approach for the production of large-scale 3D mesoporous metal oxide networks with high specific surface area and large pore volume by a facile FA-derived polymerization-carbonization-combustion (FAPCC) approach. Seven types of single-component 3D mesoporous metal oxide networks have been prepared by this method, including SnO₂, WO₃, Fe₂O₃, CeO₂, CuO, NiO, and Co₃O₄. Furthermore, multi-component metal oxide networks, such as large-scale 3D TiO₂/WO₃

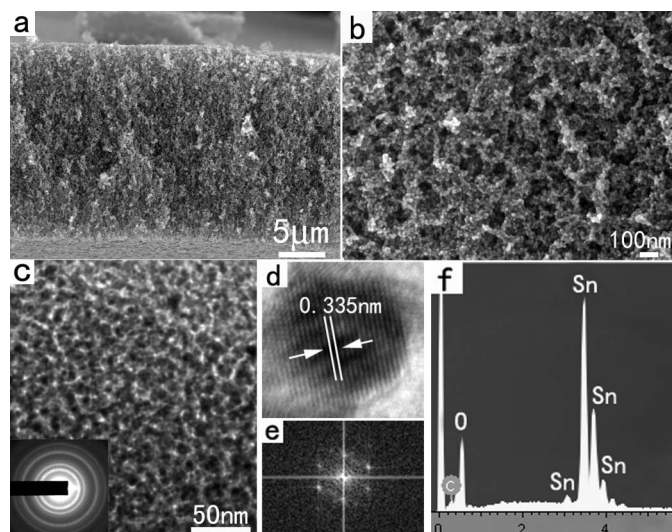


Figure 1 | (a,b) SEM images of the large-scale 3D mesoporous SnO₂ networks. (c) TEM image and the corresponding SAED pattern of the sample. (d,e) HRTEM image and the corresponding FFT pattern. (f) EDS spectrum of the sample.

mesoporous networks can also be prepared by this method. Interestingly, after slight adjustment, this method also can be used for the synthesis of large-scale 3D WO₃ and TiO₂/WO₃ hierarchical macro- and mesoporous (HMM) networks, which offers both tunable porosity and the formation of two pore networks. In addition, well-defined noble metal nanoparticles loaded large-scale 3D mesoporous metal oxide networks also can be synthesized by this present method. The important characteristics make the FAPCC stratagem become a versatile method for the design and synthesis of catalysts and catalyst supports in chemistry and catalysis.

Results

Scheme S1 outlines the typical synthesis of the large-scale 3D mesoporous metal oxide networks. In the case of synthesis of large-scale 3D mesoporous SnO₂ networks, SnCl₄, ethanol (anhydrous) and FA were mixed together to form a yellow transparent solution at room temperature. This as-obtained solution was then heated to 90 °C with a slowly rate of 1 °C min⁻¹ and was maintained at this temperature for

8 h in air. During this process, due to the Lewis acid catalytic effect of the Sn⁴⁺ ions, the FA monomer gradually polymerizes into cross-linked FAR. Such crosslinked FAR contains abundant functionalized hydroxyl (OH), therefore, Sn⁴⁺ ions would bind the OH groups through a coordination effect during the polymerization process, forming a homogenous hybrid FAR-Sn composite. Finally, carbon component in the FAR-M composite is removed by combusting and Sn⁴⁺ ions are densified to form large-scale 3D mesoporous SnO₂ networks.

SEM images clearly reveal the large-scale 3D mesoporous structure of the as-prepared SnO₂ sample (Figure 1a,b), which like a “sponge”. Generally, nanomaterials synthesized by wet-chemistry method are dispersed in solvents; thus, complicated separation processes are needed to collect the solid powders, and agglomerations may occur which leads to reducing of surface areas. The FAPCC method shown herein offers a facile way to synthesize mesoporous solid materials directly in large scales. The crystal structure and phase composition of the mesoporous products were obtained by using X-ray powder diffraction (XRD). The typical powder XRD pattern displayed in Figure S1 identifies these 3D mesoporous “sponges” as the rutile phase of SnO₂ (JPCDS No. 41-1445), and no other crystalline impurities were detected in the synthesized product. TEM image further demonstrates the interior of the “sponges” is composed of mesoporous structures forming by the random attachment of the nanoparticles with sizes from 5–8 nm (Figure 1c). The corresponding SAED pattern (inset in Figure 1c) indicates the nanoparticles are highly crystalline. HRTEM image and corresponding FFT pattern also indicate that the SnO₂ nanoparticles are highly crystalline (Figure 1d and 1e). The energy-dispersion X-Ray spectroscopy (EDS) characterization (Figure 1f) confirms that the as-synthesized mesoporous sponges are composed of only tin and oxygen. Furthermore, Raman spectra characterizations for the as-synthesized samples demonstrated that the 3D mesoporous SnO₂ networks have high crystallinity and purity (Figure S2). The G and D Raman modes of the turbostratic carbon phase were not detected, which confirmed the carbon has been completely removed.

The specific surface area, pore structures, and size distributions of the free-standing 3D mesoporous SnO₂ networks are characterized by nitrogen adsorption and desorption isotherms at 77 K (Figure 2 and Table S1). The Brunauer-Emmett-Teller (BET) surface area of the SnO₂ sponges is 185 m² g⁻¹. The SnO₂ sponges show a typical type-IV isotherm, characteristic of mesoporous materials, with an average Barretl-Joyner-Halenda (BJH) pore diameter of 4.6 nm and

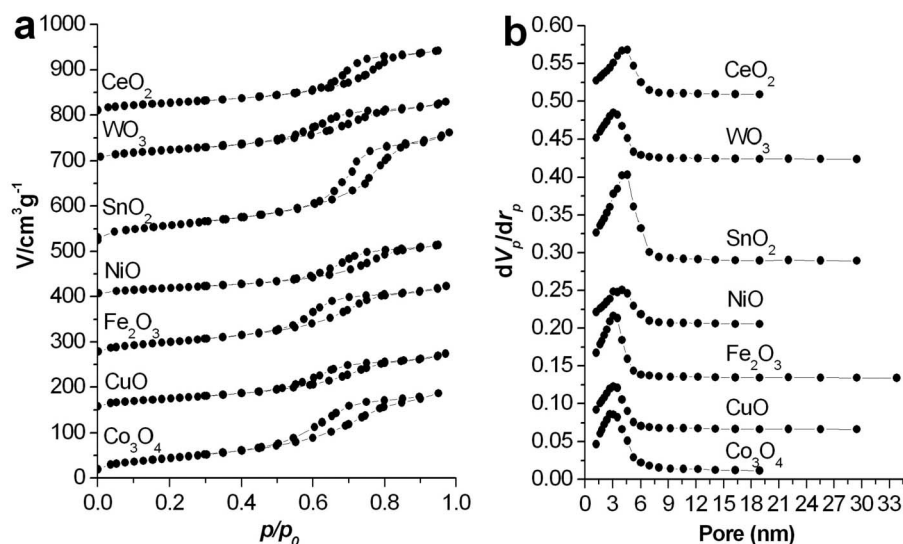


Figure 2 | (a) Nitrogen adsorption-desorption isotherm plot and (b) Pore size distribution of the as-synthesized samples: CeO₂, WO₃, SnO₂, NiO, Fe₂O₃, CuO, Co₃O₄.

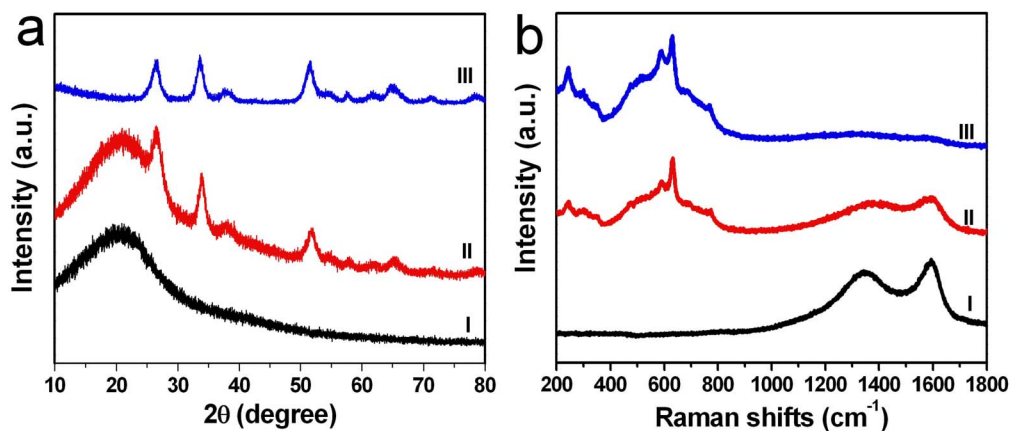


Figure 3 | XRD patterns (a) and Raman spectra (b) of the initial precursors and intermediate products of the 3D porous SnO₂ networks. I: hybrid FAR–Sn composite, II: 3 h reaction, III, IV: 6 h reaction.

a total pore volume of 0.31 cm³ g⁻¹. The high BET surface area and large total pore volume strongly support the fact that the SnO₂ sponges have a mesoporous structure. The characterization results demonstrated that the synthesis of well-defined large-scale 3D mesoporous SnO₂ networks can be achieved via the current FAPCC approach.

The material formation process was studied in more detail by carrying out the reactions at various reaction steps (Figure 3). Sn⁴⁺/FAR precursor was heated to 500°C at the rate of 1°C min⁻¹. The products were characterized after different times in the heating process. Before heating, the Sn⁴⁺/FAR precursor is a black solid. XRD pattern (pattern I in Figure 3a) and Raman spectra (spectrum I in Figure 3b) demonstrate that no tin oxide contains in the Sn⁴⁺/FAR precursor. A reaction time of 3 h, the characteristic peaks of these intermediate products in Raman spectra (spectrum II in Figure 3b) suggest the formation of tin oxide. At the same time, the reduction of Raman signals of carbon reveals that the degradative oxidation of carbonaceous templates, which is also evidenced by its XRD data in figure 3a (pattern II). When the reaction time reaches 6 h, the micro-Raman spectrum (spectrum III in Figure 3b) of the products showed the typical Raman modes of the SnO₂. While the G and D Raman modes of the turbostratic carbon phase almost were not detected, which confirmed the carbon has been almost completely removed. The corresponding XRD pattern (pattern III in Figure 3a) also confirmed this.

To confirm the generality of the FAPCC strategy, other transition-metal salts were attempted to be used as the precursors. As expected, large-scale 3D mesoporous WO₃, Fe₂O₃, Co₃O₄, NiO, CuO, and CeO₂ networks were successfully prepared by this method, respectively. As shown in Figure 4a–f, the samples are all large-scale and 3D mesoporous. XRD measuring confirmed that the samples have high crystallinity and pure crystal phase (Figure S1). The samples also have high specific surface area and large total pore volume (Figure 2 and Table S1). Furthermore, EDS characterizations for the samples demonstrated that all of the 3D mesoporous metal oxide networks have balanced atomic ratios of M/O (M = W, Fe, Co, Ni, Cu, and Ce) (Figure S3). The experimental results undoubtedly confirmed that the present FAPCC route is a general method for the preparation large-scale 3D single-component mesoporous metal oxide networks.

The proportion of FA and metal salts in the precursors play crucial roles in the formation of the 3D mesoporous networks. The Lewis acid catalytic polymerization reaction between metal salts and FA yields FAR–M hybrids, which form the primary template of 3D mesoporous networks. In the absence of FA, no 3D mesoporous networks were formed, which suggested the FAR resulted from the

polymerization of FA plays the role of backbone in the formation of the 3D free-standing mesoporous networks. To further confirm this, we have also performed the synthesis of 3D free-standing WO₃ mesoporous networks using different amounts of FA while keeping other conditions unchanged. It was found that 3D free-standing mesoporous WO₃ networks with a smaller bulkiness were obtained when a smaller amount of FA (15 mL) was used (Figure S4a). When a larger amount of FA (25 mL) was used, WO₃ networks with a larger bulkiness were synthesized (Figure S4b). A further increase in the amount of FA (35–45 mL) resulted in the formation of WO₃ networks with a much larger bulkiness (Figure S4c,d). These results demonstrated that the bulkiness of the networks can be tuned by simply adjusting the amount of FA used in the reaction.

In addition to the above-mentioned single-component 3D mesoporous metal oxide networks, well-defined multi-component 3D mesoporous metal oxide networks with high specific surface area, large pore volume, and nanojunction modified pore walls also can be prepared by this FAPCC method. For example, in the case of synthesis of 3D mesoporous TiO₂/WO₃ hybrid networks, tungsten hexachloride, titanium tetraisopropoxide, absolute ethanol, and furfural alcohol were mixed together to form a claret transparent solution at

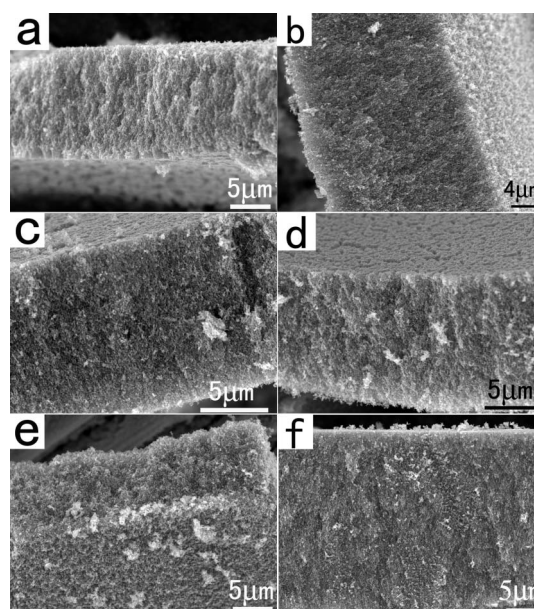


Figure 4 | SEM images of the as-synthesized 3D mesoporous metal oxide networks. (a) WO₃, (b) Fe₂O₃, (c) Co₃O₄, (d) NiO, (e) CuO, and (f) CeO₂.



room temperature. The high transparency of the precursor solution suggests it suitable for preparation of homogeneous solution of precursor.

XRD pattern shows that these as-synthesized TiO_2/WO_3 sample consist of anatase phase TiO_2 and monoclinic phase WO_3 (see the Supporting Information, Figure S5). No other crystalline products were found. A typical SEM image (Figure 5a) shows that the as-synthesized TiO_2/WO_3 products display a uniform 3D mesoporous morphology. The EDS spectroscopy shown in Figure 5b confirms that the molar ratios of these as-synthesized 3D mesoporous TiO_2/WO_3 networks are close to the initial compositions of the precursor solution. According to the EDS results, the Ti, W, and O contents in the sample are about 26.4, 23.8, and 49.8 atomic%, respectively. Furthermore, EDS elemental mapping analysis of Ti and W in Figures 5c and 5d reveal that the distribution of the two cations is very homogeneous. The TEM image further indicates that the interior of the sample is also composed of mesoporous structures forming by the attachment of the nanoparticles with sizes from 5–10 nm (Figure 5e). HRTEM image of the interface between TiO_2 and WO_3 nanoparticles is shown in Figure 5f. A distinct boundary is visible and no transitional layer is found. The HRTEM image also indicates that the hybrid pore walls are highly crystalline and possess a nanojunction structure, which is very useful in photogenerated charge separation²⁶.

Pore structures and size distributions of the TiO_2/WO_3 mesoporous networks are characterized by nitrogen adsorption and desorption isotherms at 77 K (see the Supporting Information, Figure S6). The BET surface area of the 3D TiO_2/WO_3 mesoporous networks is up to $125 \text{ m}^2 \text{ g}^{-1}$. From the nitrogen adsorption and desorption isotherms, we can see that the as-synthesized TiO_2/WO_3 networks show a typical type-IV isotherm, characteristic of mesoporous materials, with an BJH pore diameter of about 5 nm and a total pore volume of $0.17 \text{ cm}^3 \text{ g}^{-1}$. The high BET surface area and large total pore volume further demonstrated that the fact that the present FAPCC route is suitable for the synthesis of multi-component 3D mesoporous hybrids.

At the same time, we were surprised to find out that the present FAPCC method also can be used for preparation of free-standing 3D HMM nanomaterials with high yields. Scheme S2 shows the illustration of the improved FAPCC method for the synthesis of large-scale 3D HMM WO_3 networks. Briefly, in this improved method, polystyrene (PS) microspheres were used as the primary-structural

template to produce macropores, while Pluronic P123 triblock copolymer was used as the secondary-structural template to form mesopores or micropores. Furfural alcohol monomers gradually polymerized into solid FAR under the catalysis of W^{6+} ions, which act as a “concrete” to coupling the primary and secondary structural templates. A hybrid macro/mesophase was formed from the inorganic phase (tungsten hexachloride), the primary- and secondary-structural templates (PS microspheres and P123), and the structural coupling agent (furfural alcohol) via sedimentation of the PS microspheres into a close-packed solid followed by the slow polymerization of the furfural alcohol. The resulting solids were calcined to remove the organic templates (experimental details see Methods).

XRD pattern demonstrated that the obtained product is crystalline monoclinic WO_3 (Figure S7).

SEM images (Figure 6a) reveal the honeycomb-like organization of the as-synthesized sample. Figure 6b shows a magnified SEM image of the sample, which clearly displays the macroporous structure of the as-synthesized 3D WO_3 networks. The walls of the macropores are very rough and composed of numerous self-supported mesopores (Figure 6c). The mesopores partly resulted from the self-assembly of the block copolymer solution. The BET surface area of the sample is about $60 \text{ m}^2 \text{ g}^{-1}$ (Figure S8). The average mesopore diameter of the sample is 8 nm. The larger macropores (diameter > 230 nm) could not be seen because the diameter of these pores was beyond the measurement range. Hybrid TiO_2/WO_3 hierarchical porous structures also can be obtained by this method, as shown in Figure 6d. The morphology and bulkiness of the HMM networks can be facily tuned by simply changing the amount of PS microspheres used in the synthesis. For example, when smaller amount of PS microspheres were used, HMM WO_3 networks with thicker walls were obtained (Figure S9).

Noble metal particles loaded metal oxides hybrid materials have many applications²⁷. Interestingly, the present FAPCC method can be used for the synthesis of noble metal loaded porous WO_3 networks (Figure 7a). For the changes in the synthetic steps, we just need to add noble metal salts in the WO_3 precursor. From Figure 7b we can clearly see that Au nanoparticles uniformly distributed in the porous WO_3 surfaces. Furthermore, EDS elemental mapping analysis of W and Au in Figures 7c and 7d reveal that the distribution of them is very homogeneous. It should be noted that the size of most of the Au nanoparticles is very small (about 2–3 nm in di-iameter) even after the 500°C high temperature calcination, which demonstrates that the hybrid structure has high thermal stability.

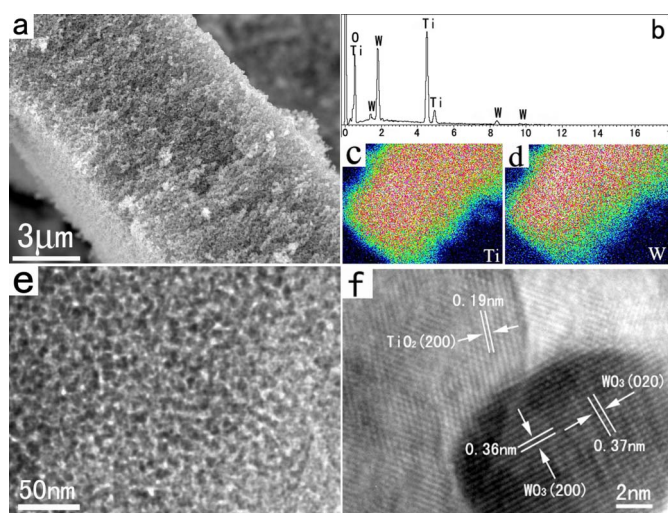


Figure 5 | (a) SEM image of the as-synthesized 3D TiO_2/WO_3 mesoporous networks. (b) EDS spectroscopy of the sample. (c) and (d) EDS elemental mapping of Ti and W, respectively. (e) and (f) Low-magnification TEM and HRTEM images, respectively.

Discussion

To demonstrate the potential application of the as-synthesized large-scale 3D mesoporous networks, we selected the 3D mesoporous WO_3

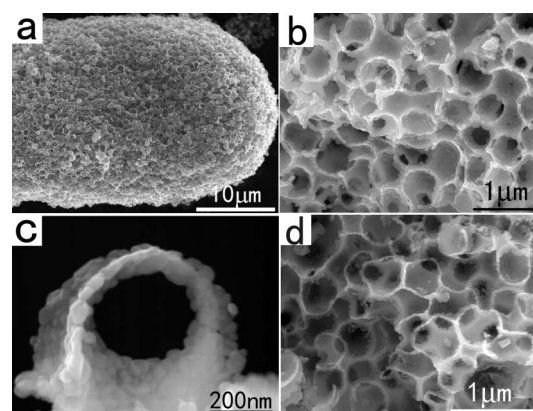


Figure 6 | (a, b) Low-magnification SEM image of the as-synthesized 3D HMM WO_3 networks. (c) High-magnification SEM image of the WO_3 networks. (d) SEM images of the HMM TiO_2/WO_3 networks.

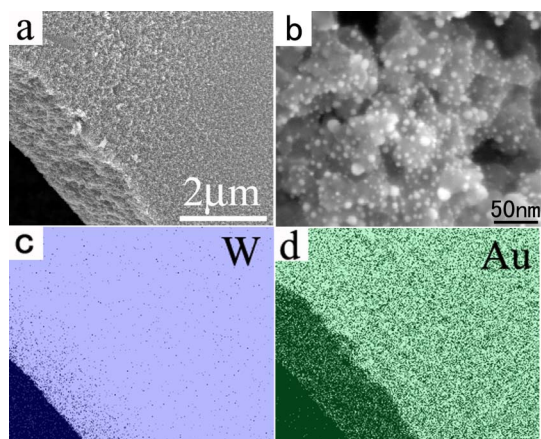


Figure 7 | (a,b) SEM images of the as-synthesized 3D porous Au/WO₃ hybrid networks. (c,d) EDS elemental mapping analysis of W and Au.

networks as photocatalysts and investigated their visible-light photocatalytic activity in the degradation of typical Azo dyes. Figure 8a shows the absorption spectra of an aqueous solution of Rhodamine B (RhB) with the WO₃ catalysts measured after exposure to visible light ($\lambda \geq 420$ nm) for different durations. As is evident, the intensity of the characteristic absorption peak of RhB gradually decreased with increasing exposure time; this indicates the photocatalytic degradation of the dye in the presence of the catalysts. After 100 min irradiation, the RhB molecules were nearly degraded. Furthermore, for another typical Azo dye, methyl orange (MO),

the photocatalytic experimental results confirmed that the 3D mesoporous WO₃ networks also has high photocatalytic activity (Figure 8b). In addition, it was observed that the photolysis of RhB and MO under visible-light irradiation was very slow, and RhB and MO molecules could not be degraded in the dark in the presence of the photocatalysts; this confirms that the photocatalytic activity indeed originated from the large-scale 3D mesoporous WO₃ network catalysts.

To further evaluate the advantage of the photocatalysis of the hybrid 3D free-standing networks, further experiments were performed under the same conditions and were aimed at comparing the photocatalytic activities of the 3D mesoporous WO₃ networks and commercial WO₃ powders (Figure 8c). For the degradation of MO molecules, the degradation efficiency of the 3D mesoporous WO₃ networks is about 3 times higher than that of the commercial WO₃ particles. When using the commercial WO₃ particles as photocatalyst (SEM image see Figure S10), the time required for complete photodegradation of MO molecules was more than 7 h. The improved degradation performance of the 3D mesoporous WO₃ networks may be attributed to their larger specific surface areas (the surface of commercial WO₃ is only about 5 m²/g), which allow them to adsorb more dye molecules and incident light. At the same time, due to the nanosized effect of the very small particles, the decrease of the bulk electron/hole (e^-/h^+) recombination and a fast interfacial charge carrier transfer, in addition to an easy charge carrier trapping, are achieved²⁸.

In addition to efficiency, stability and recyclability of photocatalysts are also important for applications. After the MO molecules are completely decomposed, centrifuging the solution enables the 3D mesoporous WO₃ networks to be easily collected to catalyze a new

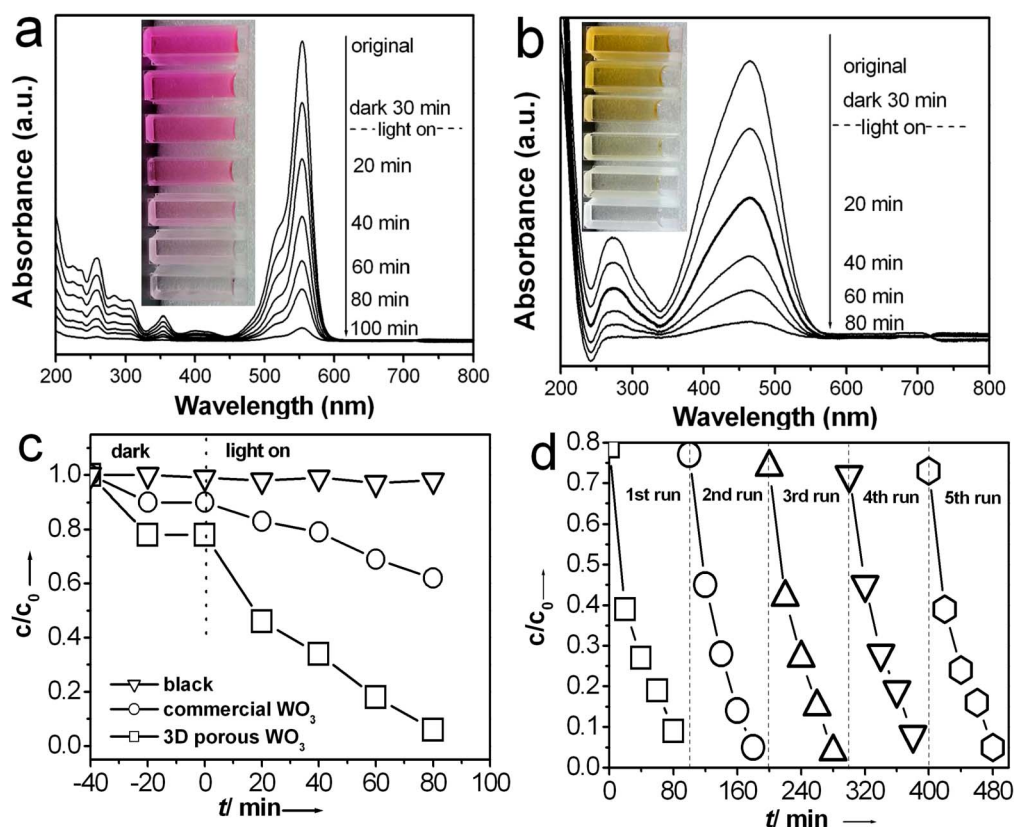


Figure 8 | (a) UV/Vis spectroscopic changes of an aqueous solution of RhB upon visible-light irradiation in the presence of the 3D mesoporous WO₃ networks. Reaction conditions: RhB concentration 10 mg/L, catalyst concentration 0.5 g/L, initial Ph 6.85, 300 W Xe-lamp ($\lambda \geq 420$ nm) with an average light intensity of 160 mW/cm². (b) UV/Vis spectroscopic changes of an aqueous solution of MO upon visible-light irradiation in the presence of the 3D mesoporous WO₃ networks. (c) The contrast of photocatalytic degradation of MO in the presence of the 3D mesoporous WO₃ and commercial WO₃ powders. (d) Recyclability of the photocatalytic decomposition of MO with the 3D mesoporous WO₃ nanomaterials.



reaction. Figure 8d plots the kinetic curves for degradation of MO solution with the use of the same experimental conditions. The 3D WO₃ mesoporous networks can be effectively recycled at least five times without an apparent decrease in its photocatalytic activity, which also demonstrates its high stability. Furthermore, the XRD patterns (Figure S11a) and UV–vis absorption (Figure S11b) demonstrated that the crystalline phase and photophysical properties of the sample after 5 cycle were not changed, which indicated its high stability. The 3D mesoporous WO₃ networks are also able to harvest sunlight to drive the degradation of RhB molecules, which is promising in practical applications such as decomposition of organic pollutants. When a mixture of the 3D WO₃ mesoporous and RhB in a glass vial is placed under the sunlight (air temperature of ~ 30°C), the red color, originating from the RhB molecules, of the solution gradually fades. The decomposition reaction is completed within 6 h (Figure S12).

In summary, we have developed a general, high-yield, and reproducible FAPCC route for the producing single-component 3D mesoporous metal oxide networks with large volume. Furthermore, this method can be used for the synthesis of multi-component 3D hybrid metal oxides. This method also can be used for the synthesis of 3D macro/mesoporous hierarchical porous materials. In addition, the present FAPCC method can be used for the synthesis of noble-metal nanoparticles loaded porous metal oxide networks. It is expected that these large-scale 3D mesoporous metal oxide networks could be promising materials for the design of various sophisticated micro/nanostructures, which could have great potential for electronic, photochemical, and catalytic applications.

Methods

Characterization. XRD patterns of the products were recorded on a Bruker D8 Focus diffractometer by using CuK α radiation ($\lambda = 1.54178 \text{ \AA}$). Scanning electron microscopy (SEM) images and EDS spectrums were obtained on a Hitachi S-4800. Transmission electron microscopy (TEM) and high-resolution TEM (HRTEM) characterizations were performed with a JEOL 2100 operated at 200 kV. BET measurements were carried out in Micromeritics Tristar 3020. UV–Vis–NIR absorption spectra were recorded with a Shimadzu UV-3600.

Synthesis of single-component 3D mesoporous metal oxide networks. In the case of SnO₂, SnCl₄ (2 g, about 7 mmol) and furfural alcohol (30 mL) were mixed together and stirred at room temperature for 20 min to obtain a transparent yellow solution. The mixture solution was then heated to 90°C with a rate of 1°C min⁻¹ and maintained at this temperature for 8 h under air, after which time a black resin was formed. Finally, the black resin was oxidized under air at 500°C for 9 h and a white cotton-like product was obtained. Other 3D mesoporous materials (WO₃, Fe₂O₃, CeO₂, NiO, Co₃O₄, CuO) have also been synthesized by this method. The general synthetic route is shown in Scheme S1.

Synthesis of multi-component 3D mesoporous metal oxide networks. In the case of synthesis of TiO₂/WO₃, 2 g of WCl₆, 2 mL of titanium tetraisopropoxide and 30 mL of furfural alcohol were mixed together and stirred at room temperature for 20 min to obtain a transparent solution. The mixture solution was then heated to 90°C with a rate of 1°C min⁻¹ and maintained at this temperature for 8 h under air, after which time a black resin was formed. Finally, the black resin was oxidized under air at 500°C for 9 h and a pale-yellow cotton-like product was obtained.

Synthesis of 3D macro/mesoporous hierarchical porous WO₃ networks. In a typical synthesis, Pluronic P123 triblock copolymer (2 g, MW = 5800) and furfural alcohol (20 mL) were mixed together and stirred at room temperature for 30 min to obtain a transparent solution. Then, a suitable amount of polystyrene (PS) microspheres was added to the solution. After that, 2.5 g of tungsten hexachloride (WCl₆) dissolved in absolute ethanol (10 mL) was added. The suspension was maintained at room temperature for 24 h, and then heated to 90°C with a rate of 1°C min⁻¹ and maintained at this temperature for 12 h, after which time a black resin was formed. Finally, the black resin was oxidized under air at 500°C for 9 h and a yellow cotton-like product was obtained. The general synthetic route was shown in Scheme S2.

Synthesis of noble metal nanoparticles loaded 3D mesoporous metal oxide networks. In the case of synthesis of 3D mesoporous Au/WO₃ networks, WCl₆ (1.5 g) and furfural alcohol (30 mL) were mixed together and stirred at room temperature for 30 min to obtain a transparent solution. After that, HAuCl₄ (0.1 g) dissolved in absolute ethanol (10 mL) was added. The mixture solution was then heated to 90°C with a rate of 1°C min⁻¹ and maintained at this temperature for 24 h under air, after which time a black resin was formed. Finally, the black resin was oxidized under air at 500°C for 9 h and a purple cotton-like product was obtained.

Photocatalytic properties test. The photocatalytic activities of the 3D mesoporous WO₃ networks were evaluated by degradation of RhB and MO in an aqueous solution under visible light from a 300 W Xe lamp (HSX-F300, NBEt) equipped with cutoff filter L42. The photocatalyst (50 mg) was poured into 100 mL RhB or MO aqueous solution (10 mg/L) in a Pyrex reactor at room temperature under air. Before light was turned on, the suspension was continuously stirred for 30–40 min in dark to ensure the establishment of an adsorption–desorption equilibrium. The concentration of RhB or MO during the degradation was monitored by colorimetry using a UV–vis spectrometer (Shimadzu UV-3600).

1. Yue, Q. *et al.* A Template Carbonization Strategy to Synthesize Ordered Mesoporous Silica Microspheres with Trapped Sulfonated Carbon Nanoparticles for Efficient Catalysis. *Angew. Chem. Int. Ed.* **51**, 10514–10518 (2012).
2. Cong, H. P. *et al.* Synthesis and Optical Properties of Mesoporous β -Co(OH)₂/ Brilliant Blue G (G250) Hybrid Hierarchical Structures. *Adv. Mater.* **24**, 1309–1315 (2012).
3. Jiang, G. L., Li, T. Y., Zhuang, J. & Wang, X. Large-scale synthesis of metastable TiO₂ (B) nanosheets with atomic thickness and their photocatalytic properties. *Chem. Commun.* **46**, 6801–6803 (2010).
4. Zhang, G. Q. & Lou, X. W. Controlled growth of NiCo₂O₄ nanorods and ultrathin nanosheets on carbon nanofibers for high-performance supercapacitors. *Sci. Rep.* **3**, DOI: 10.1038/srep01470 (2013).
5. Yang, H. G. & Zeng, H. C. Preparation of hollow anatase TiO₂ nanospheres via Ostwald ripening. *J. Phys. Chem. B* **108**, 3492–3495 (2004).
6. Zhong, Z. Y., Yin, Y. D., Gates, B. & Xia, Y. N. Preparation of mesoscale hollow spheres of TiO₂ and SnO₂ by templating against crystalline arrays of polystyrene beads. *Adv. Mater.* **12**, 206–209 (2000).
7. Wei, W. Manganese oxide-based materials as electrochemical supercapacitor electrodes. *Chem. Soc. Rev.* **40**, 1697–1721 (2011).
8. Zhu, T., Chen, J. S. & Lou, X. W. Shape-controlled synthesis of porous Co₃O₄ nanostructures for application in supercapacitors. *J. Mater. Chem.* **20**, 7015–7020 (2010).
9. Xiang, G. L., Shi, X. J., Wu, Y. L., Zhuang, J. & Wang, X. Size effects in atomic-level epitaxial redistribution process of RuO₂ over TiO₂. *Sci. Rep.* **2**, 801 (2012).
10. Zhang, G. Q. & Lou, X. W. General solution growth of mesoporous NiCo₂O₄ nanosheets on various conductive substrates as high-performance electrodes for supercapacitors. *Adv. Mater.* **25**, 976–979 (2013).
11. Chen, X. & Mao, S. S. Titanium dioxide nanomaterials: synthesis, properties, modifications, and applications. *Chem. Rev.* **107**, 2891–2959 (2007).
12. Liang, H. W. *et al.* Highly active carbonaceous nanofibers: a versatile scaffold for constructing multifunctional free-standing membranes. *ACS Nano* **5**, 8148–8161 (2011).
13. Wu, X. *et al.* Amino acid assisted synthesis of mesoporous TiO₂ nanocrystals for high performance dye-sensitized solar cells. *J. Mater. Chem.* **22**, 10438–10440 (2012).
14. Liu, G. *et al.* Synergistic Effects of B/N Doping on the Visible-Light Photocatalytic Activity of Mesoporous TiO₂. *Angew. Chem. Int. Ed.* **47**, 4516–4520 (2008).
15. Rakhi, R. B., Chen, W., Cha, D. & Alshareef, H. N. Substrate Dependent Self-Organization of Mesoporous Cobalt Oxide Nanowires with Remarkable Pseudocapacitance. *Nano Lett.* **12**, 2559–2567 (2012).
16. Wang, L. Z. *et al.* A general single-source route for the preparation of hollow nanoporous metal oxide structures. *Angew. Chem. Int. Ed.* **48**, 7048–7051 (2009).
17. Wang, Z. Y., Wang, Z. C., Wu, H. B. & Lou, X. W. Mesoporous single-crystal CoSn(OH)₆ hollow structures with multilevel interiors. *Sci. Rep.* **3**, DOR: 10.1038/srep01391 (2013).
18. Zhang, L. W., Wang, Y. J., Cheng, H. Y., Yao, W. Q. & Zhu, Y. F. Synthesis of Porous Bi₂WO₆ Thin Films as Efficient Visible-Light-Active Photocatalysts. *Adv. Mater.* **21**, 1286–1290 (2009).
19. Ge, J. J., Ding, H. P. & Xue, X. J. A nanosheet-structured three-dimensional macroporous material with high ionic conductivity synthesized using glucose as a transforming template. *Angew. Chem. Int. Ed.* **51**, 6205–6208 (2012).
20. Yu, Y. F., Zhang, J., Wu, X., Zhao, W. W. & Zhang, B. Nanoporous Single-Crystal-Like Cd_xZn_{1-x}S Nanosheets Fabricated by the Cation-Exchange Reaction of Inorganic–Organic Hybrid ZnS–Amine with Cadmium Ions. *Angew. Chem. Int. Ed.* **51**, 897–900 (2012).
21. Xiao, Z. *et al.* Facile synthesis of single-crystalline mesoporous α -Fe₂O₃ and Fe₃O₄ nanorods as anode materials for lithium-ion batteries. *J. Mater. Chem.* **22**, 20566–20573 (2012).
22. Jin, Z., Xiao, M., Bao, Z. H., Wang, P. & Wang, J. F. A general approach to mesoporous metal oxide microspheres loaded with noble metal nanoparticles. *Angew. Chem. Int. Ed.* **51**, 6406–6410 (2012).
23. Liang, H. W. *et al.* Macroscopic-Scale Template Synthesis of Robust Carbonaceous Nanofiber Hydrogels and Aerogels and Their Applications. *Angew. Chem. Int. Ed.* **51**, 5101–5105 (2012).
24. Yan, Y., Yang, H. F., Zhang, F. Q., Tu, B. & Zhao, D. Y. Surfactant-Templated Synthesis of 1D Single-Crystalline Polymer Nanostructures. *Small* **2**, 517–521 (2006).
25. Bonino, F., Damin, A., Bordiga, S., Lamberti, C. & Zecchina, A. Interaction of CD₃CN and pyridine with the Ti (IV) centers of TS-1 catalysts: a spectroscopic and computational study. *Langmuir* **19**, 2155–2161 (2003).



26. Yang, W. L. *et al.* Microwave-Assisted Synthesis of Porous Ag₂S–Ag Hybrid Nanotubes with High Visible-Light Photocatalytic Activity. *51*, 11501–11504 (2012).
27. Herzog, A. A., Kiely, C. J., Carley, A. F., Landon, P. & Hutchings, G. J. Identification of Active Gold Nanoclusters on Iron Oxide Supports for CO Oxidation. *Science* **321**, 1331–1335 (2008).
28. Bi, Y. P. & Ye, J. H. In situ oxidation synthesis of Ag/AgCl core–shell nanowires and their photocatalytic properties. *Chem. Commun.* 6551–6553 (2009).

Acknowledgements

This work received financial support from the Natural Science Foundation of China (51102220), the Science Foundation of AQSIQ (2012JK056), Dean Fund of CAIQ (2012JK023), Fund for Public Welfare Projects (201010021).

Author contributions

H.B. and X.S.L. conducted the experimental parts. C.H. and X.Z. contributed to the characterization processes. J.F.L. and Y.Y. carried out data analysis. G.C.X. designed the experiment and wrote the manuscript.

Additional information

Supplementary information accompanies this paper at <http://www.nature.com/scientificreports>

Competing financial interests: The authors declare no competing financial interests.

How to cite this article: Bai, H. *et al.* Large-Scale, Three-Dimensional, Free-Standing, and Mesoporous Metal Oxide Networks for High-Performance Photocatalysis. *Sci. Rep.* **3**, 2204; DOI:10.1038/srep02204 (2013).



This work is licensed under a Creative Commons Attribution-NonCommercial-NoDerivs 3.0 Unported license. To view a copy of this license, visit <http://creativecommons.org/licenses/by-nc-nd/3.0>